JOURNAL OF SPACECRAFT AND ROCKETS
Vol. 43, No. 6, November–December 2006

Design and Modeling of a Thermally Regulated Communications Module for Nanospacecraft

Henrik Kratz,* Mikael Karlsson,† Anders Eriksson,‡ Johan Köhler,§
Lars Stenmark,‖ and Greger Thornell¶
Uppsala University, 751 21 Uppsala, Sweden

DOI: 10.2514/1.20398

A silicon-based integrated communications and thermal management microsystem qualifying for use on Nanospace-1, a modularized microsystem-based advanced integrated nanospacecraft, is presented. The transmitter and receiver share the same module framework with essential differences only in the electronics implementation. A data rate of 1 Mbps for the transmitter and 114 kbps for the receiver is accomplished with a transmitter power for the spacecraft and ground station of 2 and 10 W, respectively. Concurrent triple usage of paraffin as low loss antenna substrate, actuator material, and heat sink is designed and analyzed for the first time. On low-power or short-time high-power dissipation of heat from the electronics, energy is stored as latent heat in this phase-change material acting as a heat sink. Thermal transport through the module is initiated by actuation of thermal switches when 75% of the paraffin's latent heat is consumed. A static thermal analysis reveals a thermal modulation factor of 5.6 between the on and off states of the thermal switches. The size of the module is 6.6 × 68 × 68 mm, and its weight is 43 g.

I. Introduction

MICROSYSTEMS for nanospacecraft are under development, and are rapidly gaining in performance and integration level. Microsystems technology (MST) is the enabling platform for miniaturized space systems. In these versatile complex systems, a design approach based on modularization of groups of diverse system functions naturally leads to the building practice of multifunctional microsystems. These are highly self-contained, and include actuators, electronics, and sensors with a low operational load on the system as a whole. A multifunctional approach involves the optimization of a multidimensional parameter space consisting of a diversity of system characteristics, e.g., power, size, weight, and complexity constraints with respect to a cost function that is openly propagated or implicitly stated in the requirements.

MST-based systems are maturing fast with respect to integration level, performance, and application spectrum. However, space systems based on micromachined silicon have mostly been for attitude control, e.g., cold/hot gas thrusters [1–3] despite the early visions of Janson et al. [4] on a miniaturized all-silicon spacecraft. Research in the field of silicon microsystems for space is vivid [5–7], and applications for miniaturized spacecraft are currently being explored [8–11].

In this paper a detailed system design and analysis of a proposed communications and thermal management module is presented. This module, probably the first of its kind, is designed for operation on Nanospace-1, the first nanospacecraft based entirely on microsystems, where it also acts as a chassis structural element and a radiation mitigation device. A design based on multiwafer silicon stack technology incorporating an antenna, electronics, a thermal radiator, a heat sink, and thermal switches enables a highly miniaturized module for advanced integrated nanospacecraft (AIN) [12]. Here, AIN implies a high performance monolithic or modularized spacecraft where some or all functions are based on MST.

The module is henceforth referred to as an "integrated communications and thermal management system for advanced integrated spacecraft," or ICTM. This paper provides a detailed design and modeling of the ICTM together with an operational description and a justification. This system is believed to fulfill the communications demand of any spacecraft with a downlink requirement in the Mbps region and also provides a generic thermal management building block for nanospacecraft. The work should be considered both an important stepping stone in the realization of a mission-specific module, and a proposal of an elaboration on a more general thermal management concept.

II. Design Concept

A. Nanospace-1 Implementation

The ICTM is designed to comply with the Nanospace-1 satellite platform [13], Fig. 1, or a similar, modularly built spacecraft. It will have true three-axis stabilization, a sun-sensor, solar cells, GPS navigation, and a monopropellant rocket engine. All modules are multifunctional, silicon-based, and manufactured using micromachining to minimize mass and increase performance.

In total there are three S-band transmitters and three S-band receivers distributed over the spacecraft to provide full antenna coverage. These are located in different modules to prevent microwave interference.

The generic orbit for Nanospace-1 is a circular low earth orbit (LEO) at 400 km altitude, although other orbits could be served after minor adjustments. A store and forward communication architecture is used where command and telemetry can be sent and gathered every time the spacecraft passes over a ground station. The command data amount is very limited (in the order of kilobytes) but the telemetry data can be quite extensive (in the order of megabytes). The latter originates from the onboard electric field vector sensor for plasma measurements.

B. Module Boundary Parameters

The miniaturized communications module operates in the complex environment of, e.g., changing information channel path

Received 21 October 2005; revision received 2 February 2006; accepted for publication 25 April 2006.

*Ph.D., The Ångström Laboratory, Ångström Space Technology Centre; henrik.kratz@angstrom.uu.se (corresponding author).
†Research Engineer, The Ångström Laboratory, Ångström Space Technology Centre.
‡Senior Scientist, The Ångström Laboratory, Ångström Space Technology Centre.
§Director, Senior Scientist, The Ångström Laboratory, Ångström Space Technology Centre.
‖Chief Technical Officer, Senior Scientist, The Ångström Laboratory, Ångström Space Technology Centre.
¶Project Manager, The Ångström Laboratory, Ångström Space Technology Centre.

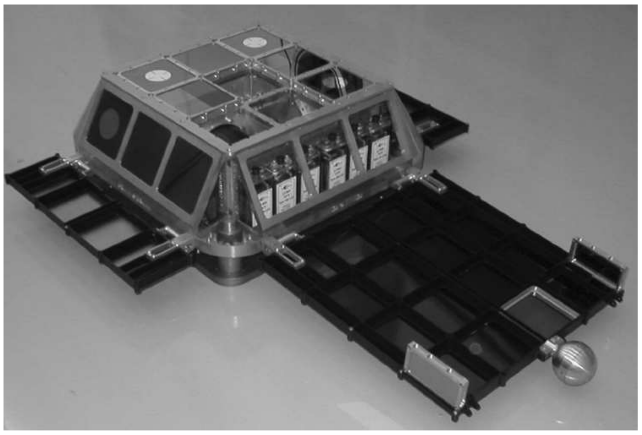

Fig. 1 A full-scale model of Nanospace-1 with panel-like microsystem modules of dimensions 68 × 68 mm.

characteristics, varying incoming solar flux, and shifting between on and off states of the heat generating electronics. The assumptions:

1) Uplink (Earth-space) frequency of 2025–2120 MHz [14]
2) Downlink (space-Earth) frequency of 2200–2300 MHz [14]
3) Maximum dc power consumption of 10 W
4) Maximum module on-time of 6 minutes
5) Minimum uplink data speed of 100 kbps
6) Minimum downlink data speed of 1 Mbps
7) Lateral dimensions of 68 × 68 mm
8) Operating temperature of −25 to 120°C
9) Chassis temperature of 15 to 37°C
10) Total mass (including casing) less than 100 g

Filtered OQPSK or GMSK is used for the S-band telemetry data, as the symbol rate exceeds 2 Msymbols/s [14]. The maximum bandwidth is 5 MHz.

C. System Functional Overview

On low-power or short-time radio transmissions, heat generated from the RF electronics will be stored not by increasing the temperature of a large thermal mass, but by supporting the latent heat of phase-change material (PCM), here being paraffin. Further heating will eventually cause melting of the paraffin to an extent where its phase-change imposed volume expansion will make its container deflect locally and trigger thermal switches. These, in turn, enable heat conduction to IR emissive surfaces (one of which is the outer side of the module itself, and a majority of which could be neighboring modules linked to the hull of the spacecraft).

The schematic cross section in Fig. 2 shows the module's two main functions, i.e., RF communications and thermal management. Thermally, three layers are distinguished: the inner part (facing the interior of the spacecraft) at a floating thermal potential, the middle part being a thermal spacer, and the top part (facing space) in thermal contact with the spacecraft shell. The heat generating electronics is embedded in the bottom part together with the thermal switches. The middle part provides the thermal insulation between the spacecraft shell and the satellite interior, and contains microwave vias, sensor vias, and thermal heat guides. Attached to the spacecraft shell is the top part where the heat guides end, and where the patch antenna and the combined thermal radiator and solar reflector are both located.

The heat guide is a high-throughput thermal conductor connected to a thermal switch. The switch modulates the heat flow through the stack and will allow for excessive heat in the integrated electronics to dissipate to the skin of the spacecraft, but also prevents sudden thermal overloading of the exterior to reach the backside of the module and the interior of the satellite. As the switches are driven by poorly conducting paraffin and based on thin, pliable members, each of them has been furnished with a special heat transfer structure consisting of a low temperature melting alloy (LMA). This structure is able to comply with the expansion of the system and yet conduct heat efficiently.

At this point it is important to realize that the top surface (to the right in Fig. 2) is in thermal equilibrium with the chassis of the

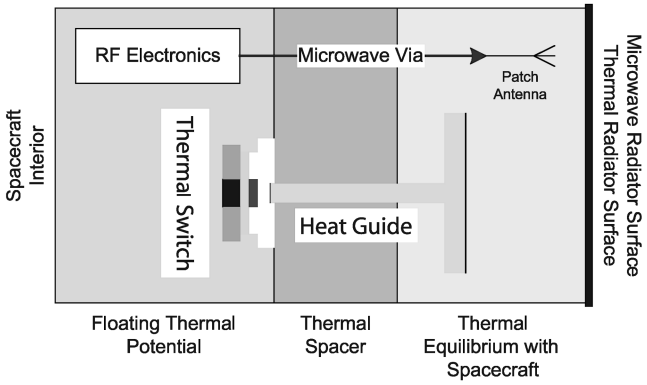

Fig. 2 RF communications and thermal management distribution through the module.

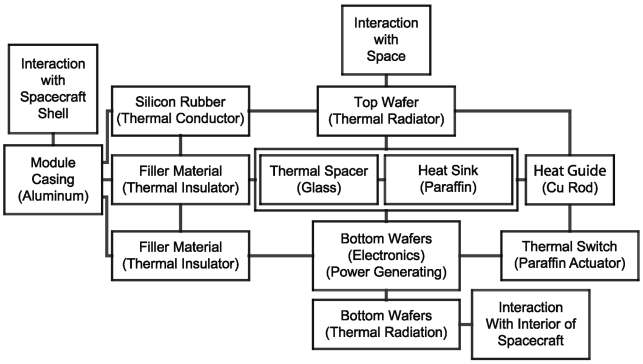

Fig. 3 A schematic overview of the thermal interactions of the ICTM module.

spacecraft, and so in thermal radiation equilibrium with space, whereas the bottom part (to the left in Fig. 2), where the heat generating RF electronics is located, will either be thermally insulated from the chassis through the thermal spacer, or in good thermal connection with the emitting surface of the module itself, as well as the chassis of the spacecraft. Any transition from the isolated to the nonisolated state, as governed by the thermal switches, will be preceded by a period of thermal storage in the bottom part of the module (to the left in Fig. 2). During this period, paraffin housed by the module's bottom part will increase its temperature until it reaches melting, where it will absorb heat to facilitate the phase transition. It is during melting that most heat is stored by the module. (The material's overall temperature will not increase much during heat storage.) Figure 3 shows the relationship between all components involved in the thermal management.

Associated with the melting of the paraffin is a large volume expansion, here employed to locally deflect the reservoir of the paraffin until it makes mechanical, and thus thermal, contact with the top part of the module. The paraffin reservoir is confined by membranes of different resilience tailored to allow a major uptake of the expansion connected with the phase transition, before bridging the thermal spacer. Most of the mechanical design issues are focused on this balancing of the membranes.

The large and distributed reservoir filled with paraffin also serves as the module's radiation shielding function.

III. Detailed Design

A. Microwave Subsystem

1. *Link Design*

The link budget for the downlink frequency band 2200–2300 MHz is based on a center frequency of 2250 MHz. A link budget can be established with the conclusion that 1 Mbps can be acheived at a bit error rate (BER) of 10^{-5} for a worst case length between the spacecraft and ground, good weather conditions, and reasonable ground station pointing accuracy. A power of 2 W is

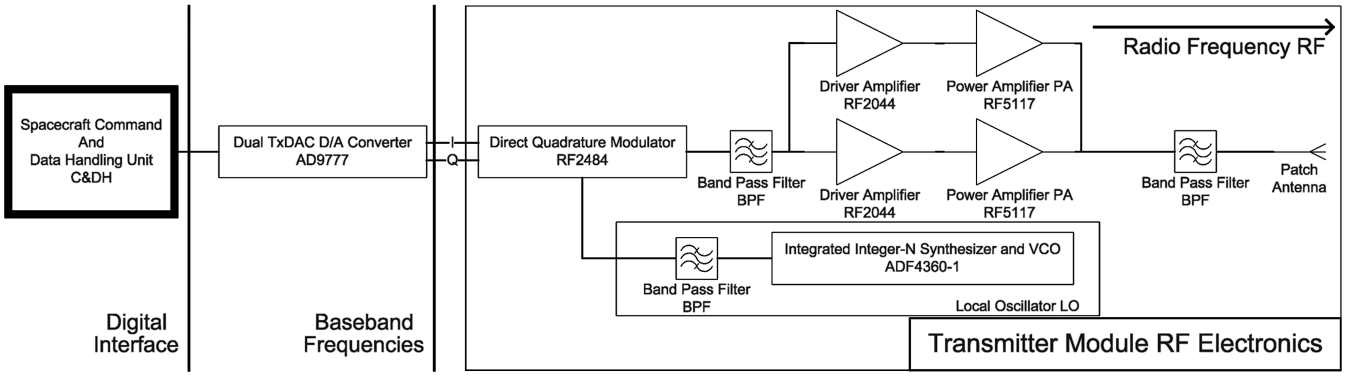

Fig. 4 The S-band transmitter electronics design.

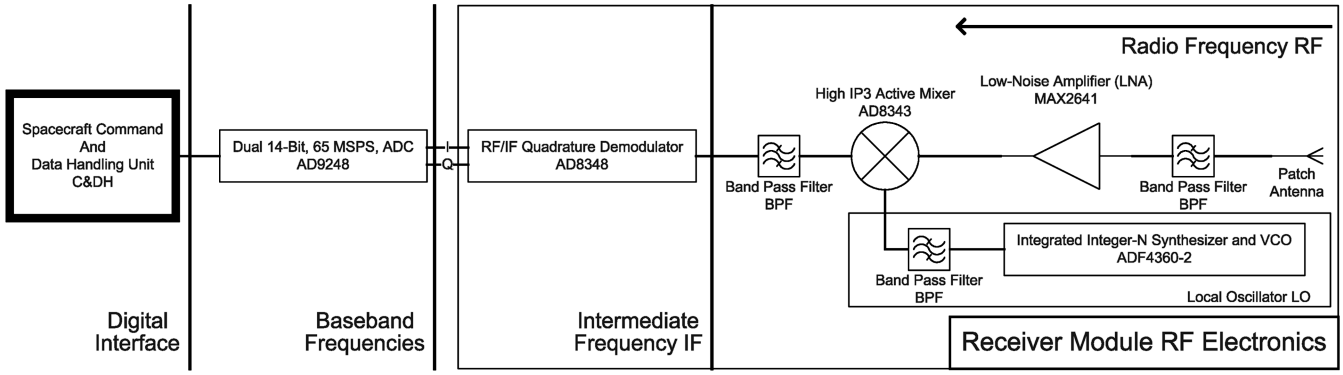

Fig. 5 The S-band receiver electronics design.

needed from the RF output to fulfill the budget, and hence roughly a maximum dc power of approximately 10 W is required assuming an average component power efficiency of 20%.

The uplink is in the band 2025–2120 MHz with a nominal design frequency of 2072.5 MHz. A link budget can be established with the conclusion that a telecommand data transfer of 114 kbps with a BER of 10^{-7} using a ground station with an RF transmitter power of 10 W is feasible.

2. *Antenna Design*

The antenna is a low-profile circularly polarized probe-fed modified disc patch with a thickness of 9 μm. To meet the requirement of circular polarization, a slot is introduced in the patch to split the current distribution into two orthogonal modes.

The multilayered substrate experienced by the antenna is 1) patch antenna: 9 μm Cu; 2) silicon: 525 μm, $\geq 8\ \mathrm{k}\Omega\,\mathrm{cm}$, bulk conductivity 0.0067 S/m, $\epsilon_r = 11.9$, $\tan\delta = 0.005$; 3) paraffin: 4 mm, $\epsilon_r = 2.3$, $\tan\delta = 0.0003$ [15]; and 4) ground layer: 9 μm Cu.

3. *Electronics*

The RF electronics of the transmitter and receiver module is to be mounted as naked chips using the thin film interconnect method of Carrillo-Ramirez and Jackson [16]. This gives a high integration level, requires no soldering steps, and provides a good thermal contact. The module electronics will interface with the spacecraft command and data handling unit (C&DH) through two coaxial MMCX (microminiature connectors) and several point contact interfaces. Functions such as data compression, encryption, and redundancy codes are implemented in the C&DH module.

The transmitter module RF electronics interfaces with the C&DH core module placed central within the spacecraft, Fig. 4. A digitalized signal enters the dual channel D/A converter that creates the analog baseband signals, the I and Q channels, that together represent the complex valued signal with amplitude and phase. The I and Q channels enter a direct quadrature modulator that has a quadrature and RF signal mixing function. A local oscillator (LO) signal is used to mix the RF signal. An integrated synthesizer, voltage controlled oscillator (VCO), and a band pass filter comprise the LO. The output of the direct quadrature modulator is fed through a bandpass filter to remove spurious frequencies generated by the nonlinear transformation in the mixer. A parallel mounted power amplifier block with both driver amplifier and power amplifier is used to amplify the RF signal. The amplified signal goes through a bandpass filter and is sent to the antenna.

The receiver electronics is shown in Fig. 5, and is similar to the transmitter design. An RF signal enters the module through the antenna and is filtered through a band pass filter before it enters a mixer that downconverts it to an intermediate frequency (IF). The mixer is fed by an LO similar to the one described in the preceding paragraph. After downconversation the signal goes through a bandpass filter and into an quadrature demodulator that takes an IF signal and mixes it down and splits the I and Q channel to two separate baseband channels. These I and Q signals enter a dual channel A/D converter and a digitized form enters the C&DH core module. The receiver structure is quite general as the decryption and error compensation algorithms reside in the C&DH.

The I and Q channels will be connected to the module by two MMCX contacts soldered to the back of the module. All other contacts will be realized by soldering patterned flexible circuit board to the back side of the module. There is a total of eight (2×4) contacts for interconnecting the temperature sensors, and 36 (9×4) contacts for interfacing the trace layer of the electronics wafer.

B. Anatomical Description

In the following, the wafers are denoted 1–5. The top wafer, no. 1, faces space and contains the patch antenna under a coating of high IR emissivity. The adjacent wafer, no. 2, is the glass wafer working as a thermal spacer and an electric insulator between the antenna and ground plane. The glass structure also contains the main paraffin cavity acting as heat storage and a low loss microwave substrate. (To the right in Fig. 6, most of the module's paraffin is shown as a disc with four handles below the glass piece.) The next two silicon wafers

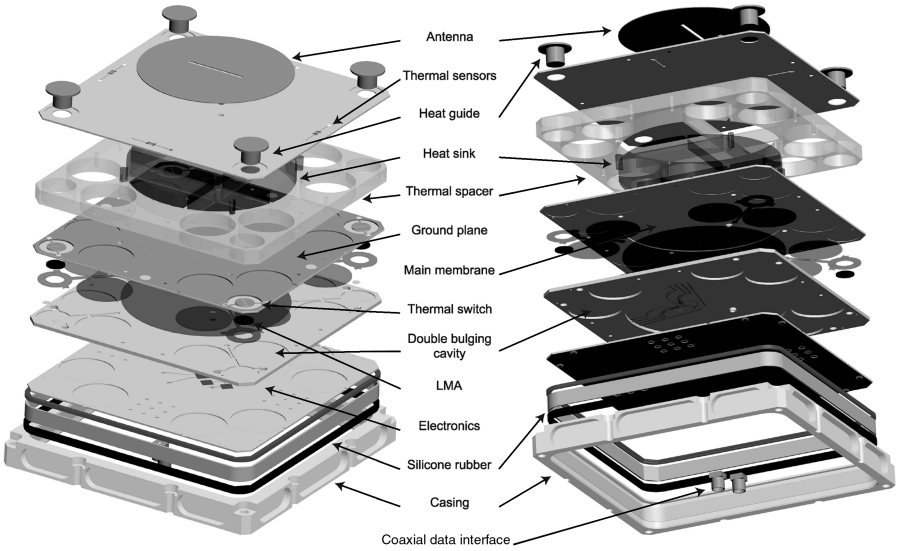

Fig. 6 Exploded front and back view of the module including mounting frame and silicone rubber gaskets.

(nos. 3 and 4) stores and dissipates heat in 12 connected circular paraffin cavities, four of which in addition are thermal switches. Wafer no. 3 also constitutes the antenna ground plane. Finally, wafer no. 5 houses RF and interface electronics.

Anodic bonding and soldering are proposed for low temperature joining of the wafers. The silicon will be structured by means of deep reactive ion etch (DRIE) [17], whereas the glass will be machined by an abrasive process, e.g., powder blasting [18].

To monitor the temperature gradient across and through the stack, four temperature sensors are located at the top of the module, one temperature sensor is located at the bottom, i.e., the electronics-containing wafer, and one at the membrane of the largest PCM cavity. All in all there are six temperature sensors, whereof three positioned at the top surface could be obsolete depending on the neighborhood symmetry. At the main membrane there is also a strain gauge to monitor the deflection. To check the status of the thermal switches, each of them has been equipped with an on/off gauge. Running through the entire wafer stack are a greater RF via connecting the antenna and the electronics, and eight lesser vias for sensor connections. On passing through the main PCM cavity, the RF via consists of a glass tube connected with four orthogonal beams to the rest of the glass wafer.

Also presented in Fig. 6 are the two silicone rubber gaskets used in clamping the module to its frame and protecting it from stress concentrations. The upper gasket will be thermally conductive in contrast to the lower one. Finally, four massive copper rods constituting the heat guides are shown at the corners of the module.

C. Implementation Particulars

Starting on the outside (facing space) and going inwards (spacecraft interior), the top wafer contains 13 holes of three different diameters. Eight are electrical vias for thermocouple elements deposited on the same side as the antenna patch, but by means of physical vapor deposition (PVD). Four flanged holes contain the copper heat guides (diameter 9 mm, length 4.8 mm) soldered to this wafer. An almost centered via is for the electrical connection of the antenna.

The thermal spacer wafer (no. 2) is of 4 mm thick glass and contains (besides the continuing vias from wafer no. 1) 13 circular cavities whereof the middle one houses paraffin, and the rest are empty to accommodate deflections of underlying membranes. Four handlelike tubes at the edge of the paraffin cavity connect this cavity with those of the underlying wafer.

The heat guides extend through the glass wafer and normally (i.e., in open mode) define a gap to the next wafer. This third wafer (no. 3) forms a perforated bottom of the main paraffin cavity where it is thinned from its backside into a membrane fixed by the RF via close

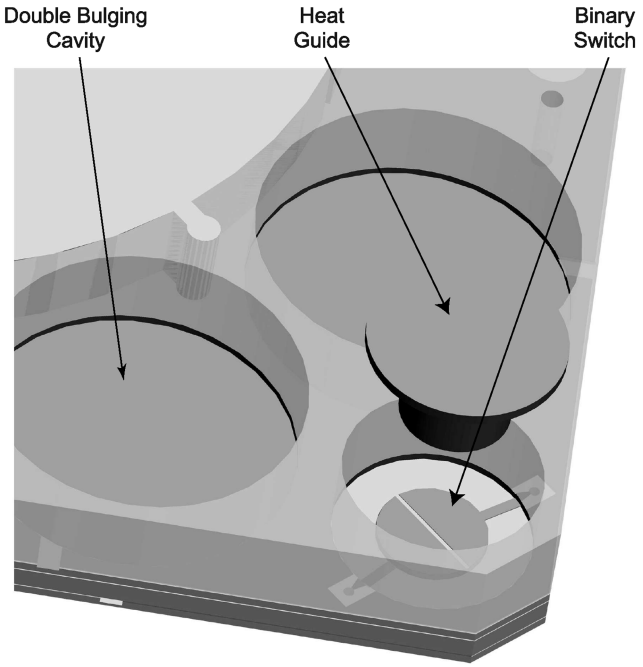

Fig. 7 A corner of the module with wafer no. 1 removed, showing two double-bulging paraffin cavities and a smaller switch cavity with sensor elements at its bottom and a heat guide above (retracted), and a small part of the main paraffin cavity (filled at the upper left).

to its center. The 45 perforations of 200 μm's width and 6 mm's pitch allow for distribution of paraffin to lower level cavities.

This wafer also constitutes the top membranes (defined from both sides of the wafer) of eight double-bulging paraffin cavities, as well as the four switch cavities containing paraffin in rings around the heat transfer structures. The switch membranes have rigid centers to accomplish good contact with the flat ends of the heat guides when the switches close. Deposited on the rigid centers are two contacts with a gap bridged by the heat guide on closing of the switch, Fig. 7. The short circuiting of this contact provides the binary output of the switch sensor.

The fourth wafer (no. 4) is thicker than the other silicon wafers, and forms the bottom of all paraffin cavities. For the eight double-bulging cavities the wafer is thinned from both sides to act as membranes. To accommodate the large deflection of the main paraffin compartment within the thickness of this wafer, the center section is thinned from the bottom side only.

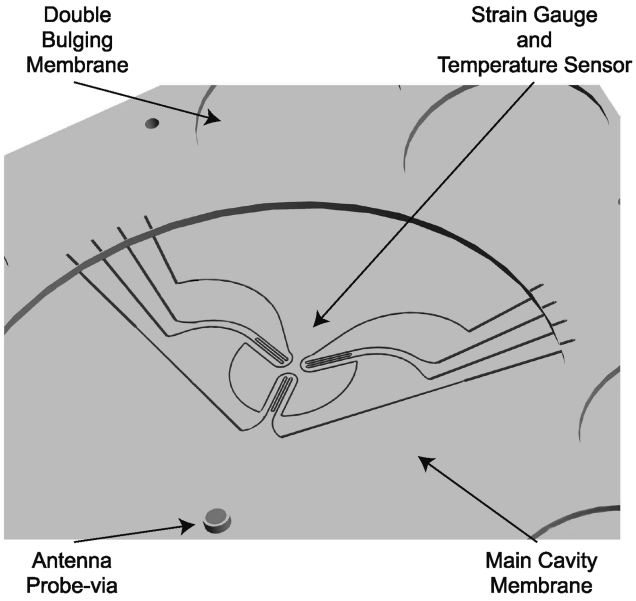

Fig. 8 Strain gauge and temperature sensor at the backside of wafer no. 3.

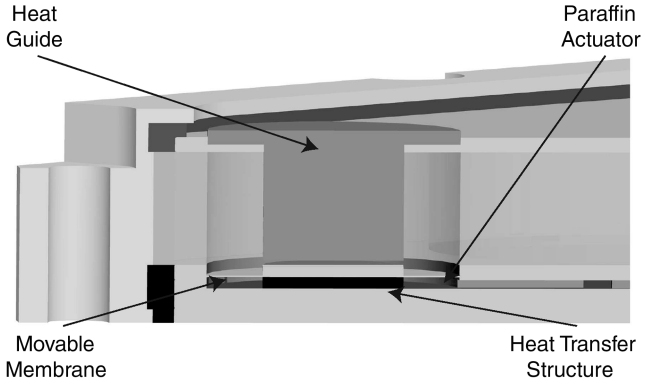

Fig. 9 Cross section of the thermal switch with its rigid center membrane controlling the thermal flow to the copper heat guide.

At the backside, and halfway at the longest distance between the RF via and the cavity's rim, i.e., where the deflection is most pronounced, a three-axial strain gauge and a thermocouple element are located; see Fig. 8.

Wafer nos. 3 and 4 both continue the electrical vias. The RF one, reaching out from the main membrane, is supported by a rim against wafer no. 4, and so prevents deflection at this point (see Fig. 8).

Wafer no. 5, finally, is also of silicon and contains eight recesses to accommodate the deflection of the bottom membranes of the double-bulging cavities on its top side, and interconnections and recesses for mounting of chips at the bottom side.

D. Thermal Switches

Because of the good thermal conductivity of silicon, heat generated in the electronics will spread through wafer no. 5 and into the adjacent paraffin cavities. The temperature of the paraffin will rise until melting is initiated, and the device enters its heat storage phase where power is consumed for latent heat. During a period of rather constant temperature, the paraffin melts and expands. The expansion is accommodated by the deflecting silicon membranes. Although the paraffin of the corner cavities melts before the material in the main compartment, their membrane deflection will not be sufficient for closure of the switches. Instead, the membrane of the main cavity will accommodate typically up to about 75% of the overall expansion, gradually become stiffer and start passing liquid paraffin to the corner cavities, finally making the four thermal switches beneath the heat

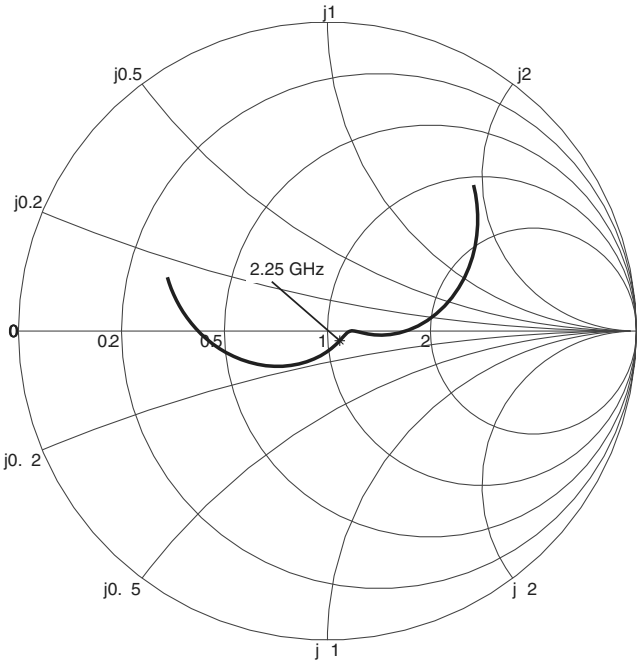

Fig. 10 A Smith diagram representation of the simulated antenna scattering parameters.

guides close, as confirmed by the switch sensors. Complying with the deflection of the switches's membranes, the already melted LMA of the heat transfer structure embedded in the paraffin of these cavities, Fig. 9, continues to thermally bridge the top and bottom of the switch cavities. On closing of the switches, heat will transfer directly to the top wafer, where a small part is emitted and a larger part dissipated through the top gasket and the frame to the chassis (for storing) and neighboring modules (for assisted emission). The distribution is monitored by the front side sensors.

E. Paraffin Filling

Filling with paraffin will be performed from the backside of wafer no. 4 via one of eight optional inlets/outlets. With a preevacuated cavity system, paraffin will flow through this wafer to fill first the nearby switch cavity, and then the two double-bulging cavities on its way to the transit through wafer no. 3, where a via brings the paraffin up to the glass wafer (no. 2) through a corresponding via. The connecting hole of the glass wafer has a slit facilitating direct filling of the (approximate) quadrant of the main cavity. Because the bottom of the main cavity is perforated, the other quadrants could be filled in a single step. However, to ensure a complete filling of the switch and double-bulging cavities in the other corners of the module, this procedure will be repeated for each inlet/outlet pair at wafer no. 4.

IV. Design Justification

A. Antenna Design

The patch antenna structure is simulated using IE3D, Zeland Software, Inc., with a trace layer consisting of a disk with a radius of 20.4 mm, a slot length of 16 mm, a slot width of 1 mm, a distance to via of 7.5 mm, and a via diameter of 1.5 mm. Scattering parameter results are presented in a Smith diagram, normalized to 50 Ω, Fig. 10. A prong can be seen where the magnitude of the orthogonal current modes are the same and good circular polarization is achieved. The expected antenna gain is shown in Fig. 11 with a maximum of 6.3 dBi at 2.25 GHz.

B. Thermomechanical Function

Fundamental to the thermomechanical design are the assumptions that the pressure is communicated through all paraffin cavities, that the heat storage function, as mainly provided by the main cavity,

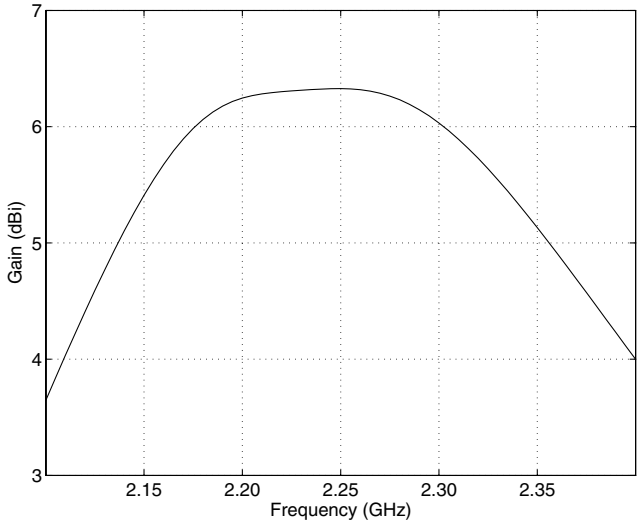

Fig. 11 Simulated antenna gain as a function of frequency.

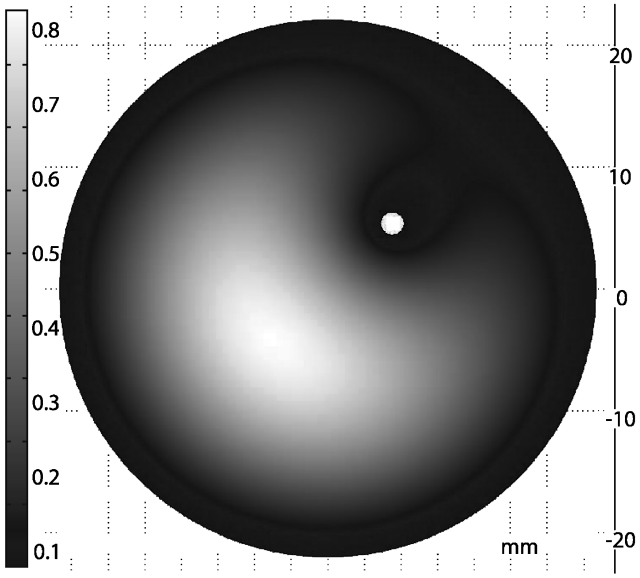

Fig. 12 Deflection of the main membrane subjected to 200 kPa.

shall execute before thermal switching, that the geometrical design shall not depend on the phase transition temperature of the paraffin, and that the exact expansion magnitude of the paraffin (typically 10–15%) shall not affect the design other than by adjustments of the membrane thicknesses: a relatively straightforward procedure in MEMS processing. Constraints other than these, stem either from what is practically attainable with respect to materials and MEMS technology, or from what is implied by the immediate demonstrator Nanospace-1, for instance the lateral size (68×68 mm) of the module, or the system requirements with, e.g., communication demands implying both the antenna size (which affects the diameter of the underlying cavity) and the transmission power governing the heat storage capacity.

Based on this, three types of cavities, heat sink or main cavity with one downward-deflecting membrane fixed by the RF via close to its center, thermal switch cavities with one upward-deflecting membrane with a rigid center (Fig. 9), and double-bulging cavities with membranes on both sides, were proposed. The total unexpanded volume of one main cavity, four switch cavities and eight double-bulging cavities is 5714 mm^3. Assuming first an effective expansion of 10%, a 75% and 100% melting of this volume implies a volume increase of 420 and 571 mm^3, respectively. Accordingly, an effective expansion of 15% gives expansions of 643 and 857 mm^3, respectively.

To set the execution order of the membranes without adding extra intelligence, it was decided to connect all cavities hydraulically. As a consequence a common pressure could be anticipated at all times.

With the only critical membrane deflection being that of the thermal switches, and given fixed diameters and a fixed activation (melting) sequence of the cavities (including an estimated threshold between the heat storage phase and the heat dissipation phase), the problem was reduced to 1) tailoring the stiffness of the three membranes separately so that the expansion of the paraffin before switching could be accommodated by the system without deflecting the switch membranes much, and 2) minimizing the corresponding strain and tailoring the structural yield strength to ensure absolutely elastic operation of the structures.

The relatively simple membranes of the thermal switch and the double-bulging cavities were treated analytically [19]. For the large center membrane, the situation was complicated by the RF via close to its center, and finite elements analysis (FEA) had to be employed.

Under the condition that the thermal switches shall activate at a melting fraction of 75%, and with the assumptions that paraffin is negligibly compressible at the pressures needed to deflect the membranes to accommodate the expansion, and that the silicon used for the housing could be treated as isotropic and assigned a yield strength (σ_y), a Young's modulus (E), and a Poisson's ratio (ν) of 7 GPa, 169 GPa, and 0.26 [20–23], respectively, the dimensioning in Table 1 was arrived at. Table 1 also contains the expansion accommodation and the corresponding maximum deflection of each cavity type at a melting fraction of 100%, and an expansion efficiency close to 10%.

At the maximum expansion of the paraffin, corresponding to a (over-) pressure of 200 kPa, the main cavity membrane was found to deflect according to Fig. 12 with a maximum of 830 μm occurring halfway at the longest distance between the rim and the RF via.

The double-bulging cavities are to assist the main cavity membrane to accommodate paraffin during operation. However, there is an uncertainty involved in the paraffin filling efficiency and in etch depth during fabrication. To account for this, a sensitivity analysis was performed. As the main cavity is responsible for the major uptake of the expansion it was investigated with respect to membrane thickness variation, Fig. 13. Furthermore, in a more generic module the via of the main cavity membrane may be relocated along its radius, and the membrane diameter altered as well, as studied in Fig. 14.

Regarding the thickness of the membranes, one could fail to etch to the specified depth, or one could obtain a thickness variation. To investigate the first case, a $\pm 15\%$ individual thickness variation was assumed for each type of membrane whereas Figs. 15 and 16 present the deflection versus pressure, and displaced volume versus pressure,

Table 1 Diameters, thicknesses, and design of the three types of membranes employed in the ICTM, their deflections, and the accommodated volumes (per membrane), when all paraffin is melted and expanded by 10%

Cavity	Main (heat sink)	Thermal switch	Double-bulging
Diameter, mm	44.0	9.00	14.5
Thickness, μm	280	50	130
Accommodated expansion, mm^3	373	9.5	222
Maximum membrane deflection, μm	820	65	250
Design	Flat, clamped, fixed close to center	Rigid center, clamped	Flat, clamped

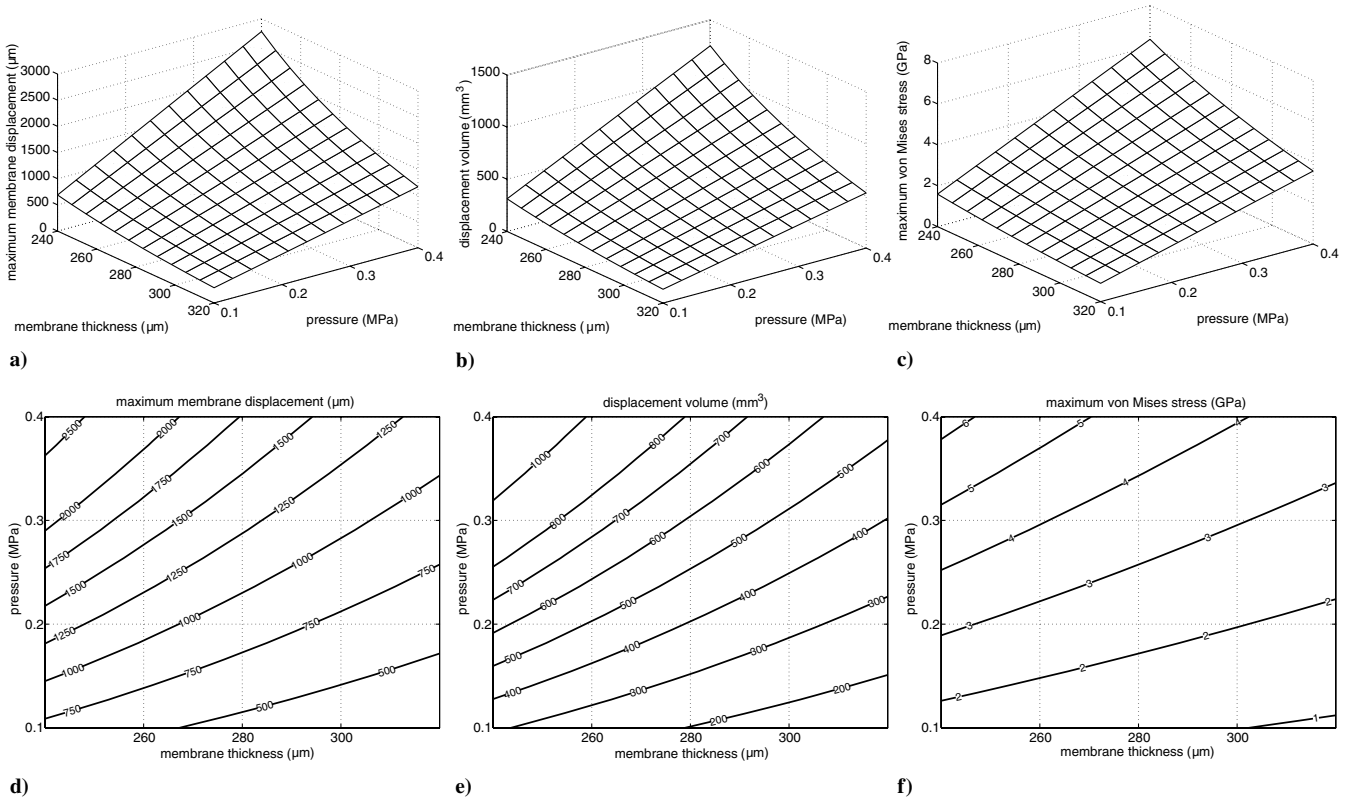

Fig. 13 a, d) Maximum membrane displacement; b, e) displaced volume; and c, f) maximum von Mises stress as a function of membrane thickness and one-sided pressure. Calculations are made with a via diameter of 1.9 mm, a membrane diameter of 44 mm, and a radial via position of 7.5 mm. Panels d), e), and f) are projections of a), b), and c), respectively.

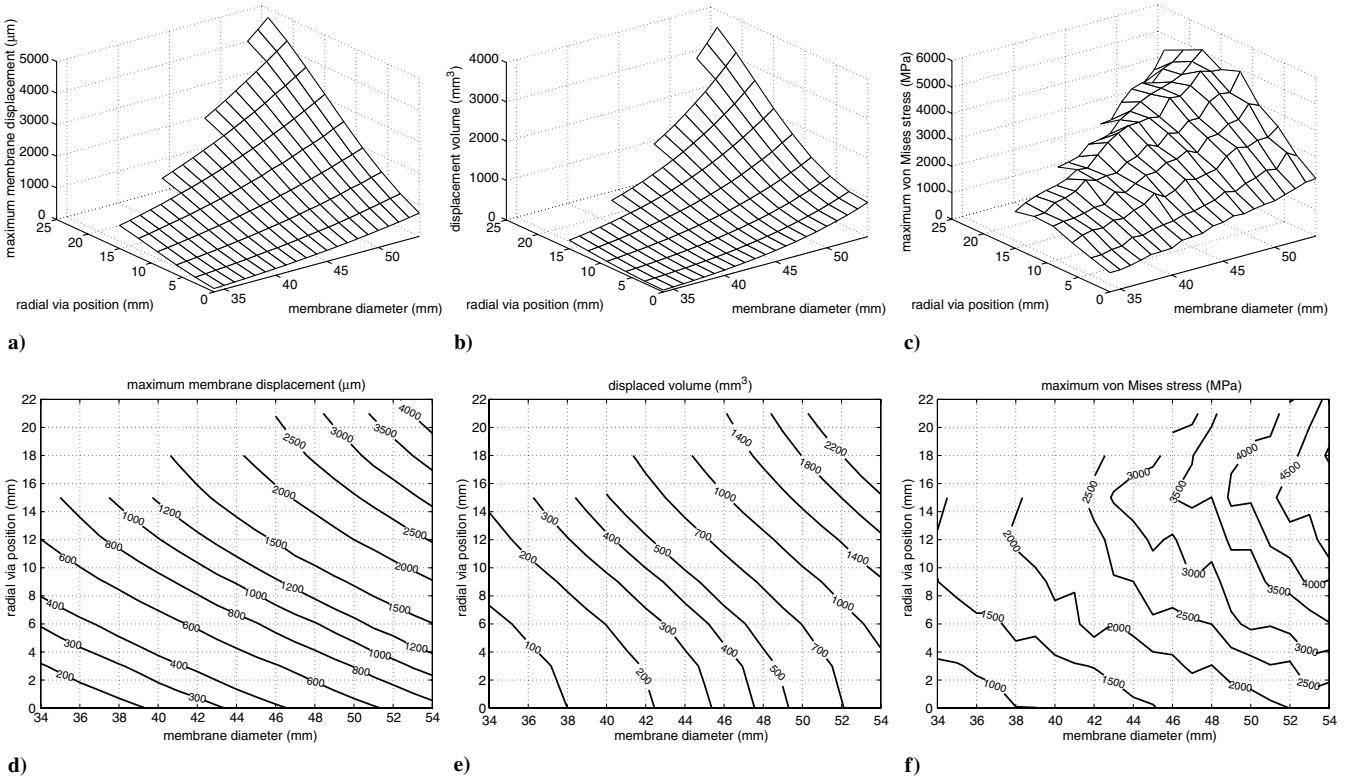

Fig. 14 a, d) Maximum membrane displacement; b, e) displaced volume; and c, f) maximum von Mises stress as a function of radial via position and membrane diameter. Calculations are made with a via diameter of 1.9 mm, a membrane thickness of 280 μm, and a pressure of 200 kPa. Panels d), e), and f) are projections of a), b), and c), respectively.

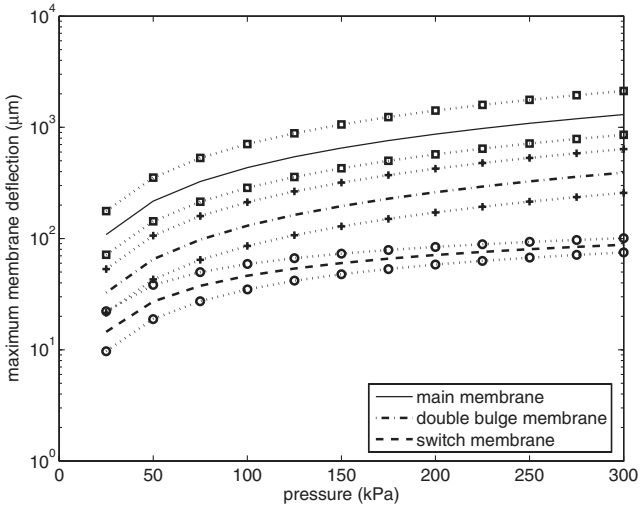

Fig. 15 Deflection vs pressure for the ICTM's three membrane types with nominal thicknesses (Table 1), and assuming a manufacturing error of +15% and −15% in membrane thickness. Above and below each nominal thickness as represented with a dashed line without markers, are the 15% thinner and thicker cases represented with dotted lines with markers (squares for the main membrane, pluses for the double-bulge ones, and circles for the switch ones).

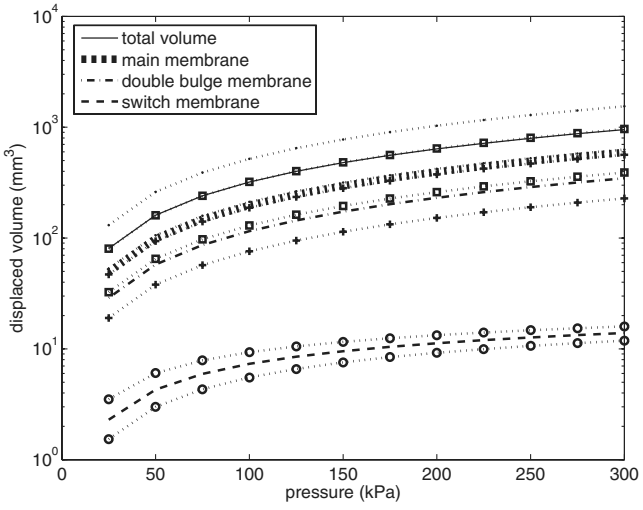

Fig. 16 Displaced volume vs pressure for the ICTM's three membrane types. In addition, a sensitivity analysis for a manufacturing error of +15% and −15% in membrane thickness has been included. (The uppermost curve represents the total volume displacement of all membranes.) Above and below the line representing the total volume, main membrane, double-bulge membrane, and switch membrane as represented with a dashed line without markers, are the 15% thinner and thicker cases represented with dotted lines with markers (small dots for the total volume, squares for the main membrane, pluses for the double-bulge ones, and circles for the switch ones).

respectively, in general for these cases, Table 2 shows a number of relevant combinations. The first cases (1–3) assume all thicknesses to be equally well or badly met. Although minor altering of the choice of paraffin could come in question to compensate for insufficient manufacturing control, none of these cases will result in failure. The two mixed cases (4–5) both fail on the other hand. Here, the thickness variations cause either a premature switch activation (4), or a lack of switch activation accompanied by a deflection override of the main membrane (5). Case 6 combines a weak switch membrane with nominally thick main and double-bulging membranes, and results in a correctly working module if a low expansion paraffin (10%) is employed. Finally, case 7 assumes nominal thickness of the main and the double-bulging membranes but a stiffer (+15%) switch membrane, and causes a deflection override of the double-bulging membranes.

C. Static Thermal Analysis

A static thermal modeling of the ICTM gives a first order of magnitude thermal performance estimate. Assessing lumped elements, based on the network shown in Fig. 3, results in a simple network of two parallel-coupled thermal conductances, $1/R_1$ and $1/R_2$, consisting of several individual elements, Table 3. The $1/R_1$ branch changes state depending on whether the switch is closed or not. The conductance $1/R_1^{\text{on}}$ describes the heat leakage through the glass spacer in parallel with the heat flow through the heat guide in series with the heat transfer structure, whereas the conductance $1/R_1^{\text{off}}$ only represents the leakage through the glass spacer. The $1/R_2$ branch simply describes the heat flow through the main paraffin cavity. From this, and with values from Table 3, R_1^{on}, R_1^{off}, and R_2 become 0.40, 2.26, and 13.2 K/W, respectively. These, with the difference in temperature between the top wafer, T_{top}, and the melting point of the paraffin, T_m, described by

$$T_{\text{top}} - T_m = -\frac{2 + \text{sgn}(q_{\text{bot}})}{4} q_{\text{bot}} (R_1^{-1} + R_2^{-1})^{-1}$$

where sgn is the signum function, and q_{bot} is the power dissipated from the electronics, residing in the bottom wafer, give the graph in

Table 2 Sensitivity analysis of thickness variations of the ICTM's module membranes

	Thickness variation									
	Switch membrane			Main membrane			Bulge membrane			
Case	−15%	0%	+15%	−15%	0%	+15%	−15%	0%	+15%	Outcome
1. All nominal		✓			✓			✓		Working
2. All thin	✓			✓			✓			Working
3. All thick			✓			✓			✓	Working
4. Mixed	✓				✓				✓	Malfunction (premature switch activation)
5. Mixed			✓	✓			✓			Malfunction (no switch activation, deflection override)
6. Mixed	✓				✓			✓		Working
7. Mixed			✓		✓			✓		Malfunction (deflection override)

Table 3 Values for the lumped thermal elements and their origin

Component	Material	Thermal conductivity, $J \cdot m^{-1} \cdot s^{-1} \cdot K^{-1}$	Thickness, mm	Area, mm^2	Resistance, K/W	Conductance, W/K
Heat guide	Copper	384 (at 300 K) [24]	4.1	19.6	0.544	1.84
Glass spacer	Borofloat	1.12 (at 90°C) [25]	4.0	1580	2.26	0.44
Heat sink	Paraffin	0.21 (in solid phase) [26]	4.0	1450	13.2	7.59×10^{-2}
Heat transfer structure	LMA	14.5 [27]	0.4	19.6	1.40	0.71

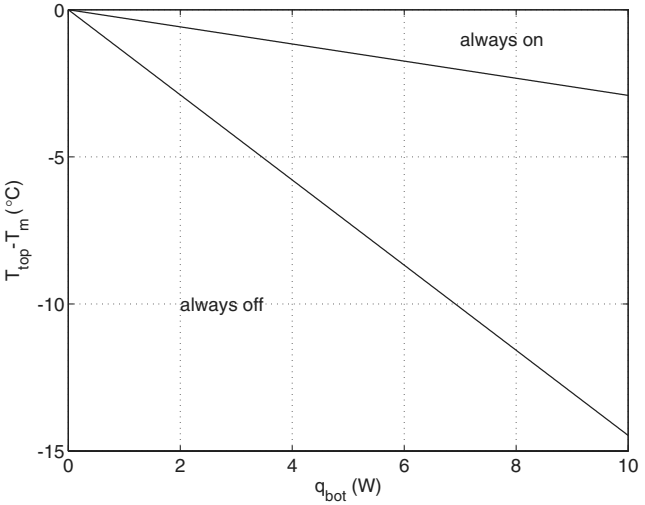

Fig. 17 Static thermal behavior with the difference in temperature of the top wafer, T_{top}, and the melting point, T_m, of the paraffin shown as a function of the generated power, q_{bot}.

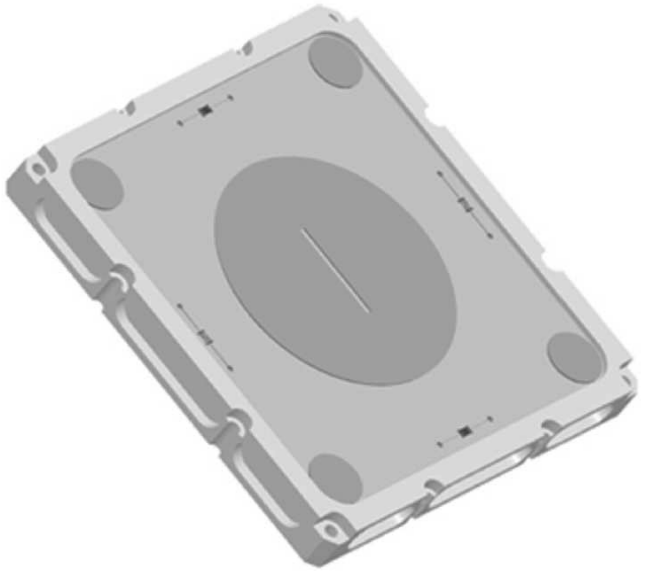

Fig. 18 Front side of the framed 68 × 68 mm module with its centered patch antenna and four corner-positioned heat guides.

Fig. 17. This indicates two stable regions where the switches are either always on or always off, whereas transient simulations are needed to characterize the intermediate region.

For a power generation of 10 W in the electronics wafer, the static model hence predicts a difference between the top wafer temperature and the melting temperature of the paraffin of 2.9 and 14.5°C for the limiting cases of thermal switch always on and off, respectively, Fig. 17. In addition, the thermal modulation of the module, here defined as the ratio of the thermal conductances in the on and off states, as represented by R_1^{on} and R_1^{off}, amounts to 5.6.

V. Discussion and Conclusions

Basically, the ICTM module, Fig. 18, is a system with a total weight of 43 g and a size of 6.6 × 68 × 68 mm comprising an RF part with a patch antenna, electronics and interconnections, and a two-step thermal management function increasing the performance of the module with respect to weight and envelope compared to solutions based on separation of the two; see, for example, [28–31]. The paraffin makes a threefold contribution to the multifunctionality of the system. First, it acts as a low loss and low dielectric constant substrate for the patch antenna [32]. Second, thermal storage is provided by the large latent heat of the material. Finally, its expansion during melting is used to mechanically alter the thermal conductance of the middle layer of the module by a factor of 5.6 according to static thermal modeling. For a 10 W heat dissipation in the electronics layer the temperature of the top wafer will be 2.9°C and 14.5°C above the PCM's melting point with the thermal switch on and off, respectively.

Figures 13 and 14 broaden the concept by showing the effect of changing the via position, the main membrane diameter and/or thickness, and the pressure. This indicates a possible implementation with other types of functions, e.g., solar sensors, solar cells, and GPS. Ultimately, a spacecraft with a thermal shell with controlled heat flow and heat storage needless of other thermal control, e.g., heat pipes or MEMS louvres is anticipated.

Electronics schematics for both the transmitter and the receiver is outlined. A signal chain ranging from the C&DH, analog/digital converters, to the module is described including the digital and analog interfaces.

The IR radiative and solar reflective properties of the top wafer could be increased with a dedicated surface coating or structuring.

The ICTM module, placed on several parts of a spacecraft hull, is expected to fulfill the communications demand of any spacecraft with a downlink requirement in the Mbps region. The link budget allows for an uplink at 114 kbps with a BER of 10^{-7} using an Earth transmitter with 10 W RF output power. As for the downlink, a high data rate of 1 Mbps with a BER 10^{-5} is achieved with a RF output of 2 W from the ICTM transmitter. With 4 mm paraffin as an antenna substrate, the antenna gain is 6.3 dBi. Earth observations, space research, and spacecraft cluster experiments are some of the missions available for the ICTM.

A thorough description of the ICTM design and its justification have been provided here. Future work includes further modeling of this system, and, more important, its realization.

Acknowledgment

The European Space Agency (ESA) is acknowledged for supporting this work financially within the Multifunctional Micro/Nano System project (ESA contract number 17704/03/NL/CH).

References

[1] Eriksson, A., and Stenmark, L., "Cold Gas Micro Thrusters—Final Edition," AIAA Paper 2002-5765, Sept. 2002.

[2] Williams, K., Eriksson, A., Thorslund, R., Köhler, J., Boman, M., and Stenmark, L., "Micro-Coil Heaters for Improved Performance in Cold/Hot Gas Microthrusters in Silicon," *3rd International Workshop on Micro and Nanotechnology for Power Generation and Energy Conversion Applications (Power MEMS)*, 2003, pp. 53–56.

[3] Köhler, J., Bejhed, J., Kratz, H., Bruhn, F., Lindberg, U., Hjort, K., and Stenmark, L., "A Hybrid Cold Gas Microthruster System for Spacecraft," *Sensors and Actuators A (Physical)*, Vol. A97–98, April 2002, pp. 587–598.

[4] Janson, S., Helvajian, H., and Robinson, E., "The Concept of "Nanosatellite" for Revolutionary Low-Cost Space Systems," International Astronautical Federation Paper IAF-93-U.5.573, 1993.

[5] Kratz, H., Öiefors, E., and Stenmark, L., "Micromachined S-band Patch Antenna with Reduced Dielectric Constant," *Sensors and Actuators A (Physical)*, Vols. 130–131, Aug. 2006, pp. 478–484.

[6] Böhnke, T., Edoff, M., and Stenmark, L., "Development of a MOEMS Sun Sensor for Space Applications," *Sensors and Actuators A (Physical)*, Vols. 130–131, Aug. 2006, pp. 28–36.

[7] Shan, X. C., Wang, Z. F., Jin, Y. F., Wu, J., Hua, J., Wong, C. K., and Maeda, R., "Studies on a Micro Combustor for Gas Turbine Engines," *Journal of Micromechanics and Microengineering*, Vol. 15, 2005, pp. S215–S221.

[8] Zencik, R. G., Jr., and Kohlhepp, K., "GPS Micro Navigation and Communication System for Clusters of Micro and Nanosatellites," *2001 IEEE Aerospace Conference Proceedings*, Vol. 5, IEEE, Piscataway, NJ, 2001, pp. 2515–2522.

[9] Bushuev, D., Kedar, D., and Arnon, S., "Analyzing the Performance of a Nanosatellite Cluster-Detector Array Receiver for Laser Communication," *Journal of Lightwave Technology*, Vol. 21, No. 2, 2003, pp. 447–455.

[10] Esper, J., Neeck, S., Slavin, J., Wiscombe, W., and Bauer, F., "Nano/Micro Satellite Constellations for Earth and Space Science," *Acta Astronautica*, Vol. 52, Nos. 9–12, May–June 2003, pp. 785–791.

[11] Esper, J., Panetta, P., Ryschkewitsch, M., Wiscombe, W., and Neeck, S., "NASA-GSFC Nano-Satellite Technology for Earth Science Missions," *Acta Astronautica*, Vol. 46, Nos. 2–6, Jan.–March 2000, pp. 287–296.

[12] Kratz, H., Köhler, J., and Stenmark, L., "Nanospacecraft Technology and its Predicted Consequences for the Space Community," *IEEE Transactions on Aerospace and Electronic Systems*, (submitted for publication).

[13] Bruhn, F., Köhler, J., and Stenmark, L., "Nanospace-1: The Impacts of the First Swedish Nanosatellite on Spacecraft Architecture and Design," *Acta Astronautica*, Vol. 53, Nos. 4–10, Aug.–Nov. 2003, pp. 633–643.

[14] Anon., "Space Engineering: Radio Frequency and Modulation," European Cooperation for Space Standardization (ECSS) Paper ECSS-E-50-05A, Jan. 2003.

[15] Haas, R., and Zimmermann, P., "22-GHz Measurements of Dielectric Constants and Loss Tangents of Castable Dielectrics at Room and Cryogenic Temperatures," *IEEE Transactions on Microwave Theory and Techniques*, Vol. MTT-24, No. 11, 1976, pp. 881–883.

[16] Carrillo-Ramirez, R., and Jackson, R., "A Highly Integrated Millimeter-Wave Active Antenna Array Using BCB and Silicon Substrate," *IEEE Transactions on Microwave Theory and Techniques*, Vol. 52, No. 6, 2004, pp. 1648–1653.

[17] Madou, M. J., *Fundamentals of Microfabrication*, 2nd ed., CRC Press, Boca Raton, FL, 2002.

[18] Wensink, H., Jansen, H., Berenschot, J., and Elwenspoek, M., "Mask Materials for Powder Blasting," *Journal of Micromechanics and Microengineering*, Vol. 10, No. 2, 2000, pp. 175–180.

[19] Giovanni, M., *Flat and Corrugated Diaphragm Design Handbook*, Marcel Dekker, New York, 1982.

[20] Petersen, K. E., "Silicon as a Mechanical Material," *Science and Technology of Microfabrication*, Vol. 76, Materials Research Society, Pittsburgh, PA, 1987, pp. 99–110.

[21] Petersen, K. E., "Silicon as a Mechanical Material," *Proceedings of the IEEE*, Vol. 70, May 1982, pp. 420–457.

[22] Franca, D., and Blouin, A., "All-Optical Measurement of In-Plane and Out-of-Plane Young's Modulus and Poisson's Ratio in Silicon Wafers by Means of Vibration Modes," *Measurement Science and Technology*, Vol. 15, May 2004, pp. 859–868.

[23] Wortman, J., and Evans, R., "Young's Modulus, Shear Modulus and Poisson's Ratio in Silicon and Germanium," *Journal of Applied Physics*, Vol. 36, Jan. 1965, pp. 153–156.

[24] Preston, S., Bretherton, I., and Forty, C., "The Thermophysical and Mechanical Properties of the Copper Heat Sink Material Intended for use in ITER," *Fusion Engineering and Design*, Vol. 66–68, 2003, pp. 441–446.

[25] SCHOTT, "BOROFLOAT Borosilicate Float Glass," *Product Information*, Aug. 2005, http://www.schott.com.

[26] Csikos, R., Keszthelyi, S., Mozes, G., and Freund, M., *Paraffin Products: Properties, Technologies, Applications (Developments in Petroleum Science)*, Elsevier Science, New York, 1983.

[27] Anon., "METSPEC 141 Alloy," *MetalSpecialities*, MCP Metal-Specialties, Inc., Fairfield, CT, http://www.mcp-metspec.thomasregister.com/ [cited 24 Aug. 2006].

[28] Yazawa, K., Solbrekken, G., and Bar-Cohen, A., "Thermoelectric-Powered Convective Cooling of Microprocessors," *IEEE Transactions on Advanced Packaging*, Vol. 28, No. 2, 2005, pp. 231–239.

[29] Cao, L., Krusius, J., Korhonen, M., and Fisher, T., "Transient Thermal Management of Portable Electronics Using Heat Storage and Dynamic Power Dissipation Control," *IEEE Transactions on Components, Packaging, and Manufacturing Technology, Part A*, Vol. 21, No. 1, 1998, pp. 113–123.

[30] Krishnan, S., and Garimella, S., "Thermal Management of Transient Power Spikes in Electronics—Phase Change Energy Storage or Copper Heat Sinks?" *Transactions of the ASME. Journal of Electronic Packaging*, Vol. 126, No. 3, 2004, pp. 308–316.

[31] Zhang, H., Pinjala, D., Joshi, Y., Wong, T., Toh, K., and Iyer, M., "Fluid Flow and Heat Transfer in Liquid Cooled Foam Heat Sinks for Electronic Packages," *IEEE Transactions on Components and Packaging Technologies*, Vol. 28, No. 2, 2005, pp. 272–280.

[32] Lamb, J. W., "Miscellaneous Data on Materials for Millimetre and Submillimetre Optics," *International Journal of Infrared and Millimeter Waves*, Vol. 17, Dec. 1996, pp. 1997–2034.

P. Huseman
Associate Editor